



Two-Dimensional Multigroup Diffusion Transport for Charged Particles in ICF Targets

J. Yuan and G.A. Moses

June 2003

UWFDM-1207

FUSION TECHNOLOGY INSTITUTE
UNIVERSITY OF WISCONSIN
MADISON WISCONSIN

DISCLAIMER

This report was prepared as an account of work sponsored by an agency of the United States Government. Neither the United States Government, nor any agency thereof, nor any of their employees, makes any warranty, express or implied, or assumes any legal liability or responsibility for the accuracy, completeness, or usefulness of any information, apparatus, product, or process disclosed, or represents that its use would not infringe privately owned rights. Reference herein to any specific commercial product, process, or service by trade name, trademark, manufacturer, or otherwise, does not necessarily constitute or imply its endorsement, recommendation, or favoring by the United States Government or any agency thereof. The views and opinions of authors expressed herein do not necessarily state or reflect those of the United States Government or any agency thereof.

**Two-Dimensional Multigroup Diffusion
Transport for Charged Particles in ICF Targets**

J. Yuan and G.A. Moses

Fusion Technology Institute
University of Wisconsin
1500 Engineering Drive
Madison, WI 53706

<http://fti.neep.wisc.edu>

June 2003

UWFDM-1207

Abstract

A two-dimensional multigroup diffusion equation for particle transport has been solved using Kershaw's differencing scheme. For the charged particle mean free path and the stopping power, we apply the form that includes the effect of large-angle scattering and also the effect of electron degeneracy in the Coulomb logarithm. The differencing scheme is first tested using a simple δ source problem having an analytical solution. Then we compare the energy deposition to ions and electrons with Corman's model. Finally, the two-dimensional multigroup diffusion module in the computer code DRACO for charged particle transport is benchmarked by performing realistic thermonuclear burns. We reproduce results for three cases from the paper by G. S. Fraley, E. J. Linnebur, R. J. Mason, and R. L. Morse (The Physics of Fluids, Vol. 17, 474, 1974), that is, volume ignition with and without a fixed boundary, and central spark ignition and propagating burn (however, under the framework of a two-dimensional scheme). Good agreement is achieved.

1. Introduction

Bootstrap heating by deposition of charged particle energy produced in the fusion reaction (especially, alpha particles in the case of deuterium-tritium (DT) fuel) back to the fusion plasma is important for burn ignition in order to achieve thermonuclear energy [1,2]. The simplest approach to the energy deposition is based on the approximation of local energy release. This approach assumes that the particles have a very short mean free path so that they are stopped as soon as they are generated. For thermonuclear burn, this condition is not fulfilled since the mean free path of fast charged particles is comparable to the size of the target under compression. Therefore, the nonlocal characteristic of thermonuclear energy release should be taken into account. Two methods are often used for transport of the charged particles. Under the condition that the mean free path is shorter than the hydrodynamic scale length, the diffusion approximation applies. With the energy variable discretized by groups, a multigroup diffusion equation is usually solved with flux limit modification. The alternative Monte Carlo method provides a more accurate approach by tracking the time and spatial evolution of the charged particle [3]. Unfortunately, this approach is computationally expensive, especially for multidimensional simulations. In this work, we use the multigroup diffusion method.

There are several different schemes for differencing the diffusion operator in the diffusion equation on the quadrilateral meshes associated with Lagrangian hydrodynamics codes, such as the cell-centered variational and finite-difference methods [4,5,6] based on a smooth mapping between the logical mesh and the spatial coordinates, and finite element methods that do not require smooth mapping but need the unknowns at the cell corners. The finite element methods [7] pose considerably more difficulty in coupling with standard Lagrangian hydrodynamic codes than the finite differencing method. In this work, Kershaw's differencing scheme [4] is used. In contrast to the differencing scheme proposed by J. E. Morel, et al. [5], the diffusion matrix in Kershaw's scheme is symmetric, which costs much less computing time than solving the asymmetric matrix, as shown in Ref. 5. Also, the scheme is equivalent to the standard five-point cell-centered scheme on an orthogonal mesh and is energy conserved. However, Morel's scheme is more accurate for problems with highly skewed meshes than Kershaw's scheme.

The main purpose of this paper is to test the correctness of our Kershaw's scheme implementation within the framework of two-dimensional geometry, to illustrate energy deposition of alpha particles to both ions and electrons, and to benchmark the charged particle transport module in the computer code DRACO [8] by simulating the ICF central ignition and propagating burns in Ref. 2.

This paper is organized as follows. In Section 2, we present the formulas for stopping power and mean free path of charged particles that are required by solving the diffusion equation. In Section 3, we give the multigroup diffusion equation and Kershaw's differencing scheme. In Section 4, we present the results for the simple δ source problem, Corman's model, and also the realistic ignition burn problem. The 2-D effect is examined by adding a perturbation layer in the target configuration.

2. Stopping power for charged particles

The stopping of charged particles from fusion reactions is a mechanism whereby charged particles deposit their kinetic energy back into the pellet so that the ignition burn propagates into the outer main fuel

layer [2]. The stopping power measures capability of the charged particles to penetrate through the hot dense plasma. Two major approaches are applied for the theoretical calculation of the stopping power. One is based on the Bohr theory which is dependent on the impact parameter between the trajectory particle and the target atom in the classical mechanic limit and the Bethe-Bloch equation which is dependent on momentum transfer from the particle to the target in the quantum mechanical limit. The other approach is based on the Fokker-Planck equation to evaluate the collision term of the Boltzmann equation. In our work, we use the formulas derived by C. Li and R. D. Petrasso [9], which properly treats the effects of large-angle scattering as well as small-angle collisions by retaining the third-order term in the Taylor expansion of the collision operator in the Fokker-Planck equation.

There are two required quantities to solve the multigroup diffusion equation [10], as shown in the next section. One is the particle mean free path and the other is the particle relaxation time from group $g+1$ to the next lower group g . The mean free path relates to the 90 degree deflection rate given by

$$\begin{aligned}\lambda &= 2v_t t_D \\ &= \frac{E_t^2}{\pi e_t^2 e_f^2 n_f \ln \Lambda_b} \left[1 + \frac{1}{2 \ln \Lambda_b} \frac{m_f - m_t}{m_f + m_t} \right]^{-1} \left[\mu + \mu' - \frac{\mu}{2x} \right]^{-1}\end{aligned}\quad (1)$$

where the modified form of the deflection rate which includes the large-angle scattering is used, E_t is the trajectory particle energy, e_t (e_f) is the trajectory (field) particle charge, m_t (m_f) is the trajectory (field) particle mass), n_f is the number density of the field particles, $\mu = \frac{2}{\sqrt{\pi}} \int_0^{x_{t/f}} e^{-\xi} \sqrt{\xi} d\xi$ is the incomplete Gamma integral, $x_{t/f} = v_t^2 / v_f^2$ where $v_f^2 = 2kT_f / m_f$. The Coulomb logarithm $\ln \Lambda_b$ for electrons uses the formula by S. Skupsky [11],

$$\ln \Lambda_{RPA} = 0.5 [\ln(1 + \Lambda_s^2 (0.37 + 0.44\eta^2)) - 1], \quad (2)$$

which is obtained from the random-phase-approximation form of the quantum-mechanical dielectric function. Λ_s is the standard Coulomb logarithm ($= 12mT / \hbar^2 k_D^2$). The effect of electron degeneracy η is calculated through the relation of the Fermi integral and the electron number density,

$$n = 4\pi / h^3 (2mT)^{3/2} F_{1/2}(\eta). \quad (3)$$

The relaxation time τ_g from the upper group $g+1$ to lower group g is defined by

$$\begin{aligned}
\tau_g &= \int_{E_g}^{E_{g+1}} \frac{1}{dE/dt} dE \\
&= \int_{E_g}^{E_{g+1}} \frac{1}{(v_\varepsilon^e + v_\varepsilon^i)E} dE
\end{aligned} \tag{4}$$

where v_ε^e (v_ε^i) is the trajectory energy loss rate interacting with electrons (ions),

$$v_\varepsilon^{e/i} = \frac{2e^2 \ln \Lambda_b^2}{m_t v_t^3} \omega_{pf}^2 G(\mu), \tag{5}$$

where ω_{pf} is the plasma frequency and

$$G(\mu) = \mu - m_f \mu' / m_t + m_f (\mu + \mu') / (m_t \ln \Lambda_b). \tag{6}$$

Note in the case of alpha particle and electron interactions, $G(\mu)$ approaches $2/3 x^{3/2}$ because of the mass ratio ($\approx 10^{-4}$) and $x \ll 1$. Thus, v_ε^e is independent of the trajectory particle energy E_t . Using this observation, the above relaxation time integral can be analytically integrated:

$$\tau_g = \frac{2}{3} \frac{1}{v_\varepsilon^e} \ln \frac{v_\varepsilon^e E_{g+1}^{3/2} + A_i}{v_\varepsilon^e E_g^{3/2} + A_i} \tag{7}$$

where $A_i = e_t^2 \ln \Lambda_i \omega_{pi}^2 G^i(\mu) \sqrt{m_t/2}$. Using the relationship between the stopping power and the energy loss rate

$$v_\varepsilon^{e/i} = \frac{v_t}{E_t} \frac{dE}{ds} \Big|_{e/i} \quad \text{and} \quad A_i = \sqrt{2/m_t} E_t \frac{dE}{ds} \Big|_i \tag{8}$$

the relaxation time τ_g can be calculated. The results of stopping power and macroscopic cross section will be given in Section 4.2.

3. Multigroup diffusion equation and numerical scheme

The multigroup equation for the charged particle diffusion [10] can be written as

$$\frac{\partial N_g}{\partial t} = \nabla \cdot D_g \nabla N_g - \frac{N_g}{\tau_g} + \frac{N_{g+1}}{\tau_{g+1}}. \tag{9}$$

The number of particles in group g is defined as $N_g = \int_{E_g}^{E_{g+1}} N_E(r, \theta, t) dE$. τ_g is the relaxation time from group $g+1$ to the next lower group g , as discussed in the previous section. The equation has a clear meaning, i.e., the change rate of the particle number in group g is equal to the summation of the rates at which particles leave the differencing volume ($\nabla \cdot D_g \nabla N_g$) and group g (N_g / τ_g), and a source term (N_{g+1} / τ_{g+1}) that represents the rate at which particles enter group g from an upper energy group $g+1$. D_g is the flux limited diffusion coefficient. The flux limiter originates from the approximation that the diffusion theory makes to close the infinite chained equations when dealing with the moment of the transport equation. By omitting the gradient of the flux, the closure equation is in the form of Fick's law. The closure equation has nonphysical behavior in the optically thin limit, that is, it has an infinite propagation velocity. To correct this problem, the flux limiter is always introduced. Several flux limiter forms exist [12]. For example, the ‘‘sum’’ flux limiter takes the form

$$D_g = \frac{v_g}{3/\lambda_g + \bar{\mu}^{-1} |\nabla N_g| / N_g}. \quad (10)$$

The average diffusion direction $\bar{\mu}$ representing the deviation from an isotropic distribution is

$$|\bar{\mu}^{-1}| = 1 + 3 \exp(-\lambda_g N_g^{-1} |\nabla N_g| / 2),$$

where λ_g is the particle mean free path with velocity $v_g = \sqrt{(E_g + E_{g+1}) / m_t}$ as defined in the previous section. Another flux limiter form used in Ref. 13 is proposed by Levermore and Pomraning (LP) [13]. In Ref. 13, the authors argue that the LP diffusion model is better than the ‘‘sum’’ form in terms of the evaluation of the ignition condition and the gain. In our work, we also use the LP flux limiter:

$$D = \xi(\beta) \lambda, \quad \xi(\beta) = \left[\coth(\beta) - \frac{1}{\beta} \right] \frac{1}{\beta}, \quad \beta = \lambda \frac{|\nabla E|}{E}. \quad (11)$$

The energy deposition to electrons (ions) is calculated using the expression

$$\dot{E}_{dep}^i = A t_E \frac{N_g}{\tau_g} \int_{E_g}^{E_{g+1}} \frac{dE}{E^{3/2} + A t_E}. \quad (12)$$

Using the mean value theorem,

$$\dot{E}_{dep}^i = A t_E \frac{N_g}{\tau_g} \frac{E_{g+1} - E_g}{E_g^{3/2} + A t_E}, \quad \dot{E}_{dep}^e = \frac{N_g}{\tau_g} (E_{g+1} - E_g) - \dot{E}_{dep}^i. \quad (13)$$

The above equations completely describe the multigroup diffusion transport. The next issue is to solve the equation numerically. There are several different schemes for solving the above diffusion equation on two-dimension quadrilateral meshes. For instance, Kershaw has developed a nine-point cell-centered differencing scheme based on the variational method. Morel and his colleagues have developed a new cell-centered diffusion scheme which is more accurate than Kershaw's scheme when the mesh is significantly skewed. However, Morel's scheme is more costly since it uses the cell-edge unknown in addition to the cell-center unknowns and the associated diffusion matrix is asymmetric. In this work, we use Kershaw's scheme. For clarity and completeness, we rewrite the matrix of Kershaw's diffusion operator and the building blocks in a way that it is easier for implementation.

The basic coordinates are denoted by R and Z to conform to the cylindrical symmetry notation. In the case of planar geometry, R corresponds to Y and Z corresponds to X . Each quadrilateral zone is labeled by the smallest (K,L) pair in contrast to the largest (K,L) pair in Ref. 4, as shown in Fig. 1.

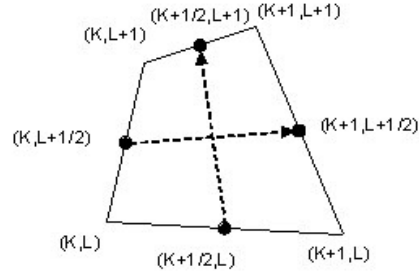


Figure 1. Labeling of the quadrilateral zone.

The zone corners are indexed by integers and the zone edge center is indexed by half integers. Following Kershaw's paper, the diagonal element and the four upper diagonal elements are

$$V_{K,L}A_{(K,L),(K,L)} = -\sigma_{(K,L)} - \sigma_{(K-1,L)} - \lambda_{(K,L)} - \lambda_{(K,L-1)} + \frac{1}{2}(\rho_{(K,L)}^{(1)} + \rho_{(K,L)}^{(2)} + \rho_{(K,L)}^{(3)} + \rho_{(K,L)}^{(4)}) \quad (14.1)$$

$$V_{K,L}A_{(K,L),(K+1,L)} = \sigma_{(K,L)} - \frac{1}{4}(\rho_{(K,L)}^{(1)} + \rho_{(K+1,L)}^{(2)} - \rho_{(K+1,L)}^{(3)} - \rho_{(K,L)}^{(4)}) \quad (14.2)$$

$$V_{K,L}A_{(K,L),(K,L+1)} = \lambda_{(K,L)} - \frac{1}{4}(\rho_{(K,L)}^{(1)} + \rho_{(K,L+1)}^{(2)} - \rho_{(K,L)}^{(3)} - \rho_{(K,L+1)}^{(4)}) \quad (14.3)$$

$$V_{K,L}A_{(K,L),(K+1,L+1)} = -\frac{1}{4}(\rho_{(K+1,L)}^{(3)} + \rho_{(K,L+1)}^{(4)}) \quad (14.4)$$

$$V_{K,L} A_{(K,L),(K-1,L+1)} = \frac{1}{4} (\rho_{(K-1,L)}^{(1)} + \rho_{(K,L+1)}^{(2)}) \quad (14.5)$$

where

$$\sigma_{(K,L)} = \Sigma_{(K,L)}^2 (\vec{B}_{(K,L)}^2 + \vec{B}_{(K+1,L)}^2) / 2 \quad (14.6)$$

$$\lambda_{(K,L)} = \Lambda_{(K,L)}^2 (\vec{A}_{(K,L)}^2 + \vec{A}_{(K,L+1)}^2) / 2 \quad (14.7)$$

$$\rho_{(K,L)}^{(1)} = \Sigma_{(K,L)} \Lambda_{(K,L)} C_{(K,L)} \quad (14.8)$$

$$\rho_{(K,L)}^{(2)} = \Sigma_{(K-1,L)} \Lambda_{(K,L-1)} C_{(K,L)} \quad (14.9)$$

$$\rho_{(K,L)}^{(3)} = \Sigma_{(K-1,L)} \Lambda_{(K,L)} C_{(K,L)} \quad (14.10)$$

$$\rho_{(K,L)}^{(4)} = \Sigma_{(K,L)} \Lambda_{(K,L-1)} C_{(K,L)} \quad (14.11)$$

$$C_{(K,L)} = \vec{A}_{(K,L)} \cdot \vec{B}_{(K,L)} \quad (14.12)$$

$$\vec{A}_{(K,L)} = \vec{R}_{(K+1,L+1/2)} - \vec{R}_{(K,L+1/2)} \quad (14.13)$$

$$\vec{B}_{(K,L)} = \vec{R}_{(K+1/2,L+1)} - \vec{R}_{(K+1/2,L)} \quad (14.14)$$

$\Sigma_{(K,L)}$ averages between zones (K,L) and (K+1,L) and $\Lambda_{(K,L)}$ averages between zones (K,L) and (K,L+1). Note $R_{(K+1/2,L+1/2)}$ is the R component of the zone center (K,L). For planar geometry, it is equal to 1.

$$\Sigma_{(K,L)}^2 = (R_{(K+1/2,L+1/2)} + R_{(K+3/2,L+1/2)}) / ((J_{(K,L)} / D_{(K,L)} + (J_{(K+1,L)} / D_{(K+1,L)}))$$

$$\Lambda_{(K,L)}^2 = (R_{(K+1/2,L+1/2)} + R_{(K+1/2,L+3/2)}) / ((J_{(K,L)} / D_{(K,L)} + (J_{(K,L+1)} / D_{(K,L+1)}))$$

J is the Jacobian of the transformation from physical mesh (R,Z) to logical mesh (K,L), and it is differenced as

$$J_{(K,L)} = (R_{(K+1/2,L)} - R_{(K-1/2,L)})(Z_{(K,L+1/2)} - Z_{(K,L-1/2)}) - (R_{(K,L+1/2)} - R_{(K,L-1/2)})(Z_{(K+1/2,L)} - Z_{(K-1/2,L)}) \quad (15)$$

Substituting the diffusion matrix A into the diffusion equation and multiplying by the volume V , we have

$$V \frac{\partial N_g}{\partial t} = AN_g - V \frac{N_g}{\tau_g} + VS_g. \quad (16)$$

Using implicit time differencing and defining $\Delta N_g^{n+1} = N_g^{n+1} - N_g^n$, the actual equation that is solved is a linear equation defined by

$$\overline{\overline{A}} \Delta N_g^{n+1} = V^n N_g^n - \overline{\overline{A}} N_g^n + \Delta t V^{n+1} S_g \quad (17)$$

where matrix $\overline{\overline{A}} = V^{n+1} - \Delta t(A - V^{n+1} / \tau_g)$.

The resulting matrix is a nine-point-non-zero banded matrix, which can be solved by using either a direct solver or an iterative solver. For problems with small mesh size, the direct Gaussian eliminating method is enough. However, for a typical ICF simulation, the mesh size easily goes up to 100 by 100 (2-D cases). Under such circumstances, the iterative solver or parallel linear system solver should be used. In our work, the PETSC parallel solver library is employed as an addition to the direct solver and the ICCG iterative solver.

4. Numerical simulation results

4.1. Testing of the scheme

We first test the correctness and the accuracy of the code. We consider a simple 1-D wave propagation problem with a heat source Q at the origin $r=0$ and time $t=0$. The diffusion equation in this case takes the form

$$\frac{\partial N}{\partial t} = \frac{1}{r^2} \frac{\partial}{\partial r} (r^2 D \frac{\partial N}{\partial r}). \quad (18)$$

The solution of this problem with linear heat conduction (constant D) is well known:

$N = Q / (4\pi Dt)^{3/2} \exp[-r^2 / (4Dt)]$. The one-dimensional spherical geometry can be simulated on a two-dimensional cylindrical mesh by degenerating the left-side edge to the origin and letting the right-side edge be the spherical surface and also imposing reflective boundary conditions for the top and bottom edges of the mesh. The comparison between the calculation and the exact solution is shown in Fig. 2.

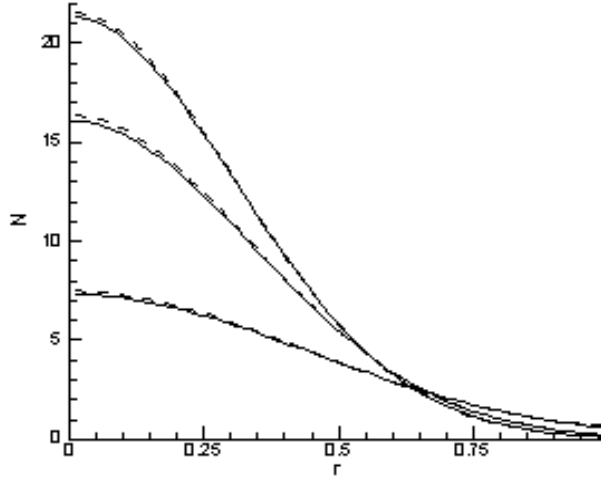


Figure 2. Comparison of the numerical simulation with the analytical solution for the δ source problem.

We can see that the calculation agrees with the exact solution very well. Having this in mind, we move forward to solve the diffusion equation for charged particle transport by plugging in the coefficients of stopping power and mean free path.

4.2. Stopping power and charged particle diffusion

The macroscopic cross section vs. energy of the injected α particle is shown in Fig. 3 at a plasma density of 3000 g/cm^3 . For ions, the cross section does not change much as a function of plasma temperature but this is not the case for electrons. As indicated in Eq. 1, the effect of temperature mainly comes from the Coulomb logarithm and the velocity ratio. The variation of the Coulomb logarithm for electrons is larger than the variation for ions when the temperature changes. Another quantity that measures the particle stopping power is the areal density $\rho\lambda_\alpha$, which is calculated as

$$\rho\lambda_\alpha = \int_0^{E_0} \left(\frac{dE}{\rho ds} \right)^{-1} dE. \quad (19)$$

Figure 4 displays this result as a function of plasma temperature for several different densities. To illustrate the effect of large-angle scattering in stopping power, we present the result in Fig. 5. We found that there is about up to 3.1% decrease in $\rho\lambda_\alpha$ contributing from pure electrons, and an almost constant 5.8% decrease contributing from pure ions, and up to a 4.7% decrease contributing from both electrons and ions.

To the best of our knowledge, there is no published report for two-dimensional charged particle diffusion that we can compare with. Therefore, we choose the 1-D spherical test problem used in Ref. 10. Again, we use the same method to simulate 1-D spherical geometry with the 2-D cylindrical mesh. The case studied is 3.5 MeV alpha particles injected isotropically in a 50 keV equimolar deuterium and tritium plasma. Following the same notation in Ref. 10, we show the time-dependent total energy deposition and its partition between electrons and ions for different groups in Fig. 6. The energy deposition to electrons

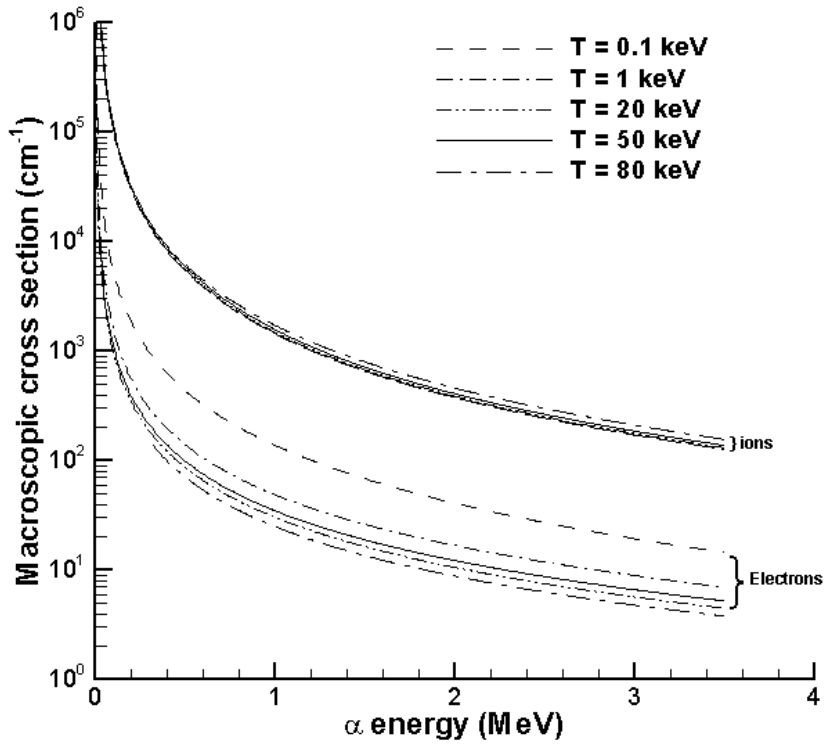


Figure 3. The macroscopic cross section vs. energy of the injected α particle.

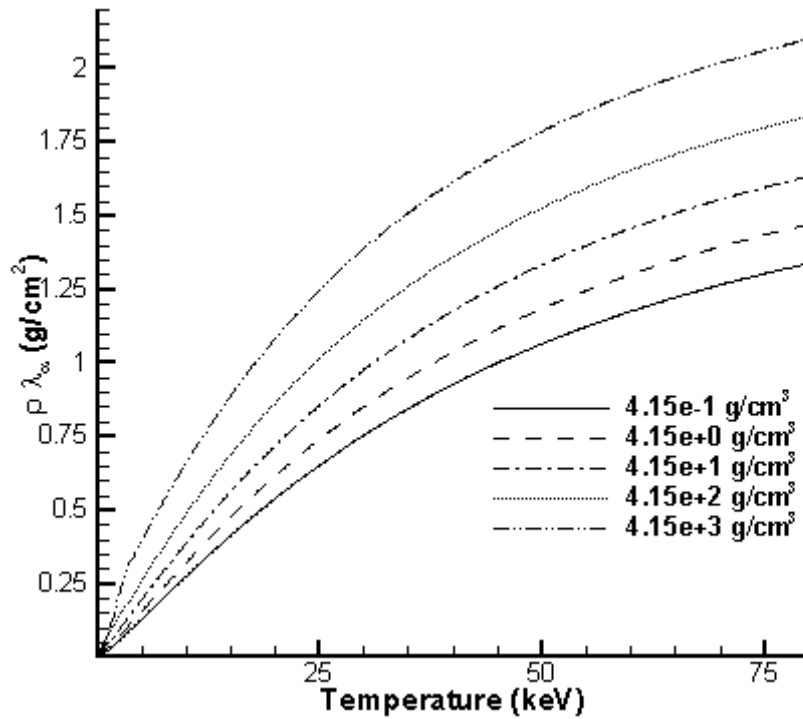


Figure 4. $\rho \lambda_{\alpha}$ as a function of plasma temperature for several different densities.

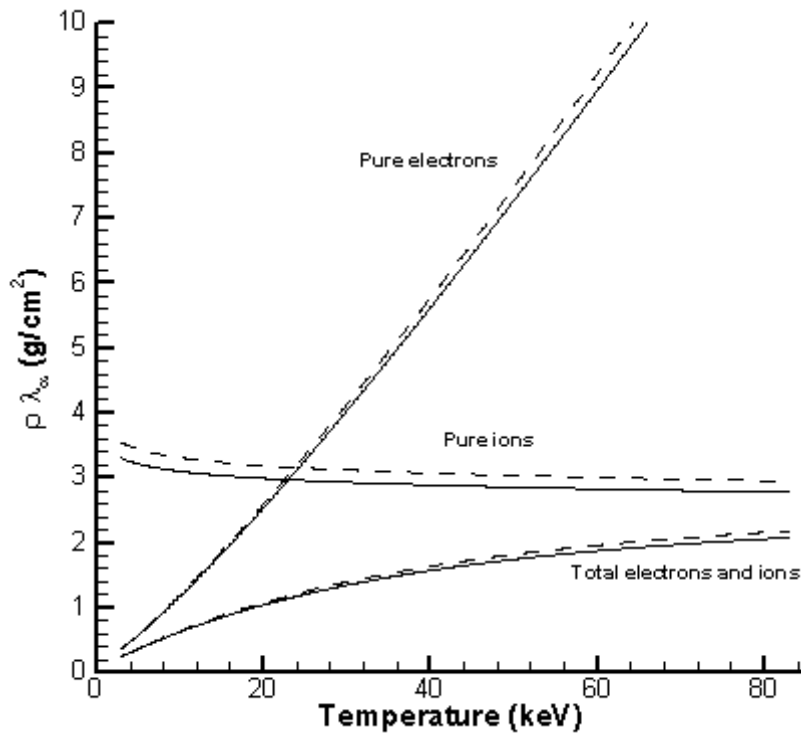


Figure 5. $\rho\lambda_{\alpha}$ for pure electron stopping, pure ion stopping and both electrons and ions. The dashed lines represent the results without the large-scattering effect in the stopping power calculation.

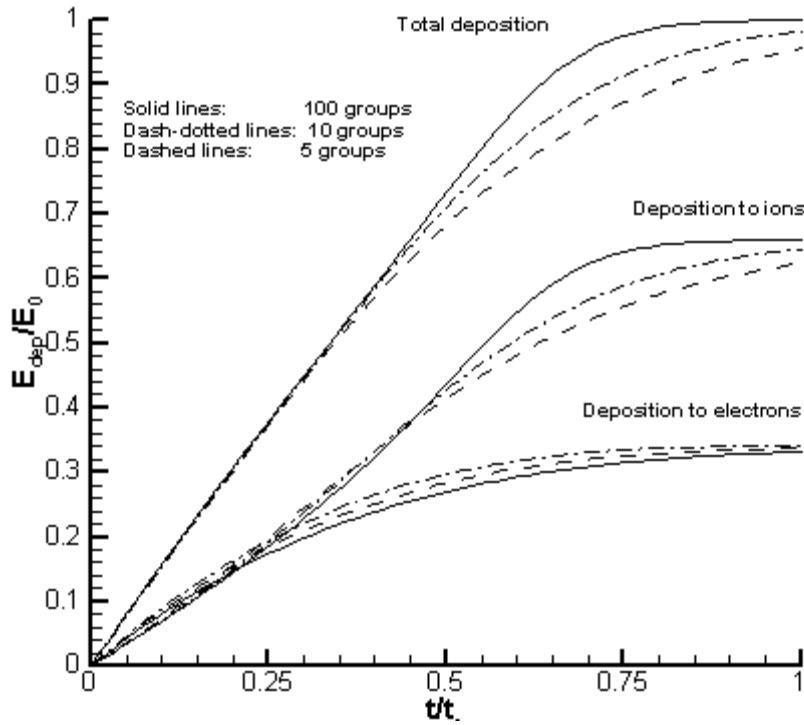


Figure 6. Energy deposition and its partitioning to electrons and ions for 3.5 MeV α particle injected into a 50 keV DT plasma.

dominates before the time ratio 0.2. After that, the energy deposition to ions surpasses the deposition to electrons. We can see that the ratio of the energy deposition to ions and electrons is 66/34, which agrees with the result in Table 1 from Ref. 9 very well.

4.3. Ignition and burn simulations

In previous sections, we first test Kershaw's scheme implementation for the two-dimensional cylindrical geometry by comparing the numerical result with the analytic solution for a simple δ source problem, then we apply the stopping power and the absorption cross section to the diffusion equation to study the time and spatial deposition of the energetic alpha particles to both ions and electrons. In this section, we perform realistic ignition and burn simulations one step further. We have implemented the above charged particle diffusion model in the computer code DRACO [8], which is an Arbitrary Lagrangian-Eulerian code designed to run in multidimensional geometry. It includes all kinds of ICF physics such as energy exchange among the fields, refractive ray tracing, classical ion and electron conductivity, multigroup radiation diffusion, and nonlocal alpha particle diffusion energy deposition. Although the code is capable of simulating the growing instability in multidimensional geometry, we instead use the code to simulate the one-dimensional problem but under the two-dimensional scheme using the same technique as above, since the purpose of this work is to verify the correctness of the implementation of Kershaw's scheme and also to study the particle energy deposition.

Three thermonuclear burn cases have been studied in Ref. 2. The first one assumes that the uniformly burning sphere has an artificially fixed boundary which means an infinite confinement time, and initially, $T = 3$ keV, $\rho = 3000$ g/cm³, and $R = 4.3 \times 10^{-4}$ cm. Our stopping power calculation gives $\rho\lambda_\alpha = 0.256$, and thus $\lambda_\alpha/R = 0.2$. Therefore, the fusion generated alpha particles are effectively recaptured. The time dependence of the cell-averaged ion and electron temperature is shown in Fig. 7. The ion temperature rises up to 100 keV by $t = 12$ ps while the electron temperature rises up to 70 keV. The energy loss through radiation begins to cool the burn after $t = 12$ ps and eventually quenches the burn. In the figure, we also plot the results from Ref. 10. We can see they agree very well.

Instead of assuming a fixed boundary condition, the second case study assumes a free boundary, which allows disassembly of the sphere. The same initial condition as above is used except $T = 20$ keV initially. The spatial ion temperature distribution with time evolution is given in Fig. 8. The sphere is heated almost uniformly up to 35 keV and then the temperature decreases gradually on the edges. At $t = 1.31$ ps, the ion temperature at the center is about 52 keV, and the sphere expands to double size of the radius. The sphere cools down after $t = 1.31$ ps and expansion terminates the burn at about $t = 4$ ps. The fuel burns up to 18%.

The third case is the central ignition and propagating burn. In order to improve the gain factor, the concept of central spark ignition and propagation burn, as an alternative to volume ignition, is investigated by many authors. For example, a 5.2-fold multiplication in the gain factor is achieved in Ref. 2. 91% of the yield of the volume ignition case is released by investing 18% of its energy with central ignition. We use the same configuration as in Ref. 2. The sphere is initially uniform at $\rho = 6000$ g/cm³ and $R = 7.4$ cm. The inner part of the sphere has a temperature of 20 keV with a radius of 3.4 cm. It contains 10% of the total mass. The temperature of the outer layer of the sphere is at 1 keV initially. Evolution of the density and ion

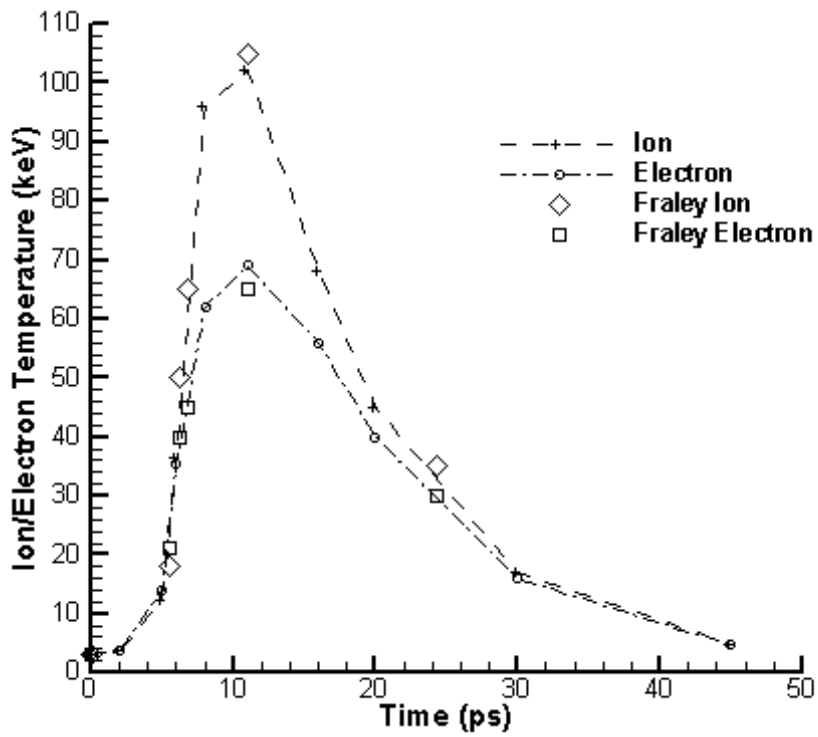


Figure 7. Time-dependence of the cell-averaged ion and electron temperature for volume ignition with fixed boundary for Fraley's [2] test case 1.

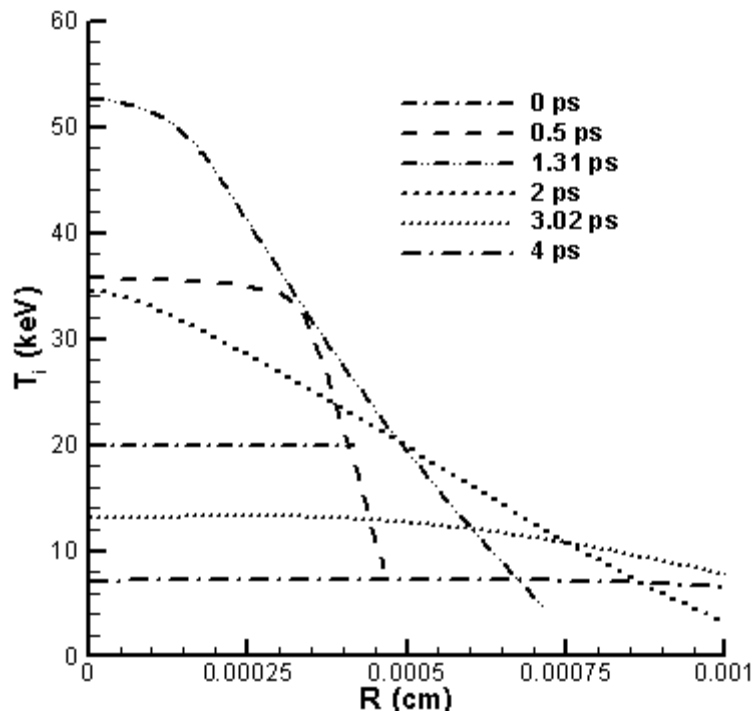


Figure 8. The spatial ion temperature distribution with time evolution for the volume ignition with free expansive boundary for Fraley's [2] test case 2.

temperature is shown in Fig. 9 and Fig. 10, respectively. The density curve at $t = 0.3$ ps depicts the process that the outer region is compressed by the inner expansion caused by the center bootstrap heating, and generates the wave-like structure. The central expansion pushes the fuel mass to the outer region, and then the outer region burns to high temperature by 1.2 ps while the center temperature decreases because of high depletion. The outer region expansion re-implodes the center at $t = 1.6$ ps and pushes the center temperature up to 175 keV. Then, the density and temperature decrease by sphere expansion and finally the burn is quenched with the fuel burning up to 40%. The above pictures agree with those in Ref. 2 very well. Finally, the 2-D effect is examined by putting a perturbation layer in the middle of the sphere. The grid setup (60 by 60) and the ion temperature contour for simulation time at 2 ps is shown in Fig. 11(a) and Fig. 11(b), respectively. Figure 11(b) shows that the perturbation in the middle is pushed to the wavefront and also amplified. The effect on the cell average ion temperature is given in Fig. 12. We can see that the perturbation seems to have little effect on the peak time (about 1.4 ps), however, the average ion temperature under perturbation is increased by 12%.

5. Summary

We have solved the two-dimensional multigroup diffusion equation for charged particle transport in Kershaw's scheme. The code is first tested against a simple δ source transport which has an analytical solution under the framework of the two-dimensional geometry. Then the equation is solved with actual diffusion coefficients. For stopping power and mean free path, we apply the form with the large-scattering modification. Comparing with $\rho\lambda_\alpha$ results calculated from the classical formulas without the large-scattering effect, we found that $\rho\lambda_\alpha$ for pure electrons, pure ions and the cumulative effects of electrons and ions with the large-scattering effect is about 3.1%, 5.8%, and 4.7% lower, respectively.

We have installed this model in the computer code DRACO, which is an ALE multidimensional code with many ICF physics. We have carried out simulations of the thermonuclear burn in DT microspheres, emphasizing the bootstrap heating and central spark ignition and propagating burn. The simulations include multigroup radiation transport, thermal transport and coupling for electrons and ions. We compare our 2-D-for-1-D results for all study cases with Ref. 2. Good agreement is found for each case in terms of the heating rate, time and spatial mass and ion temperature distribution. Running the simulation in the full 2-D calculation shows an increase of 12% of the average ion temperature under the perturbation configuration.

Acknowledgements

We thank D. Keller for the numerical support for parallel computing. The authors would like to thank LLE, University of Rochester for financial support.

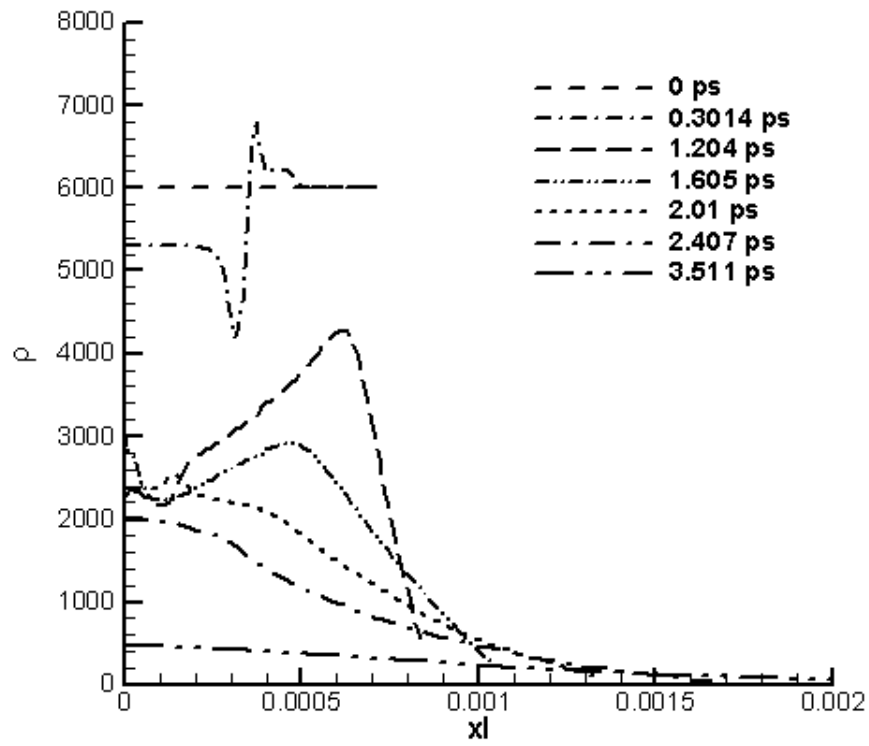


Figure 9. Evolution of the spatial density for central spark ignition and propagating burn for Fraley's [2] test case 3.

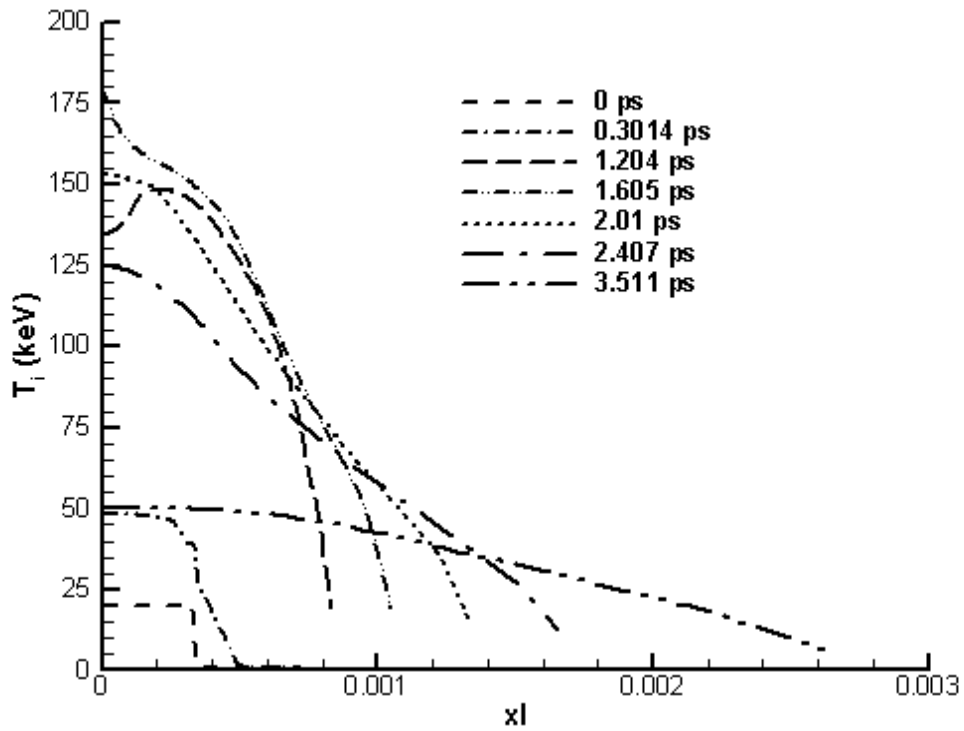


Figure 10. Evolution of the spatial ion temperature for the central spark ignition and propagating burn for Fraley's [2] test case 3.

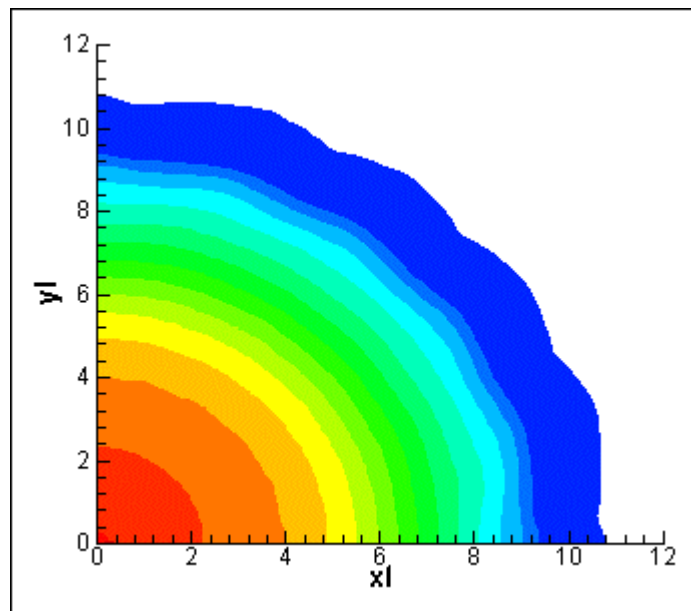
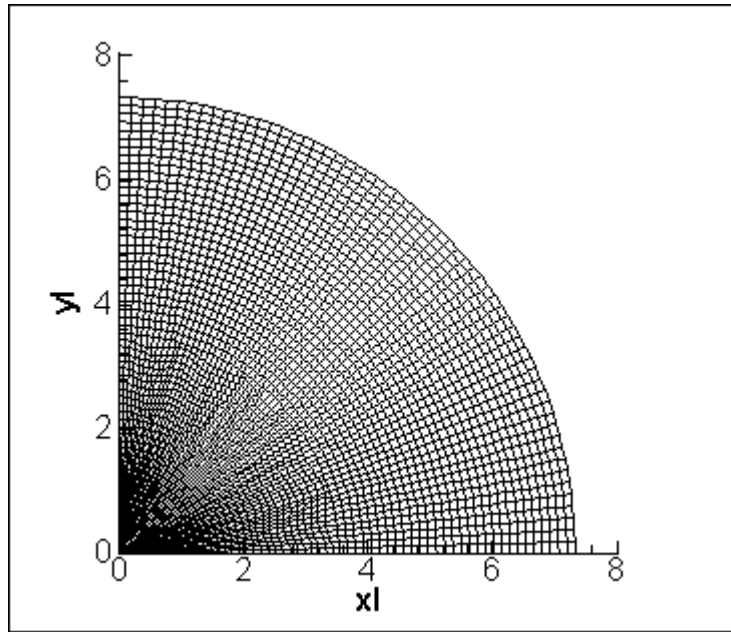


Figure 11. (a) Perturbation mesh with size of 60 by 60. (b) The spatial ion temperature with a perturbation in the middle of the sphere at time 2 ps.

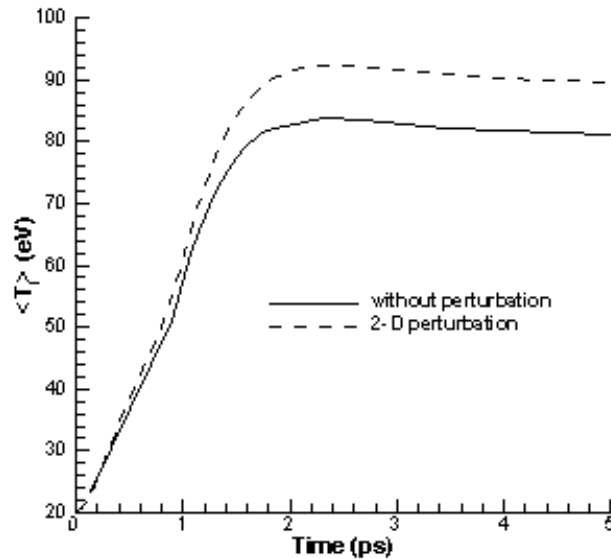


Figure 12. Comparison of the average ion temperature for the target configuration with and without perturbation.

References

- [1] J. S. Clarke, H. N. Fisher, and R. J. Mason, *Phys. Rev. Lett.*, 30, 89 (1973).
- [2] G. S. Fraley, E. J. Linnebur, R. J. Mason, and R. L. Morse, *The Physics of Fluids*, 17, 474 (1974).
- [3] M. J. Berger, "Monte-Carlo Calculation of the Penetration and Diffusion of Fast Charged Particles", *Methods in Computational Physics I*, Academic Press, NY and London (1963).
- [4] D. S. Kershaw, *J. of Comp. Phys.*, 39, 375 (1981).
- [5] G. J. Pert, *J. of Comp. Phys.*, 42, 20 (1981).
- [6] J. E. Morel, J. E. Dendy, Jr. Michael, L. Hall, and S. W. White, *J. of Comp. Phys.*, 103, 286 (1992).
- [7] I. Shestakov, J. A. Harte, and D. S. Kershaw, *J. of Comp. Phys.*, 76, 385 (1988).
- [8] D. Keller, T. J. B. Collins, J. A. Delettrez, P. W. McKenty, P. B. Rahda, B. Whitney and G. A. Moses, "DRACO – A New Multidimensional Hydrocode", *Bull. Am. Phys. Soc.*, 44(7), 37 (1999).
- [9] Chi-Kang Li and R. D. Petrasso, *Phys. Rev. Lett.*, 70, 3059 (1993).
- [10] E. G. Corman, W. E. Loewe, G. E. Cooper, A. M. Winslow, *Nuclear Fusion*, 15, 377 (1975).
- [11] S. Skupsky, *Phys. Rev. A*, 16, 727 (1977).
- [12] G. L. Olson, L. H. Auer, M. L. Hall, "Diffusion, P1 and Other Approximate Form of Radiation Transport", LA-UR-99-471, 1996.
- [13] T. Johzaki, A. Oda, Y. Nakao, K. Kudo, *Nuclear Fusion*, 39, 753 (1999).
- [14] C. D. Levermore, G. C. Pomraning, *Astrophys. J.* 248, 321 (1981).